Eclética Química Journal

Original article

revista.iq.unesp.br

| Vol. 47 | special issue 1 | 2022 |

Influence of Zr-metal-organic framework coupling on the morphology and photoelectrochemical properties of SnO_2

Letícia Guerreiro da Trindade[1+], Letícia Zanchet[2], Bianca Lins Zambon da Silva[3], Elson Longo[4], Tatiana Martelli Mazzo[3]

1. University of São Paulo, São Carlos Institute of Chemistry, São Carlos, Brazil.
2. Federal University of Rio Grande do Sul, Institute of Chemistry, Porto Alegre, Brazil.
3. Federal University of São Paulo, Institute of Marine Sciences, Santos, Brazil.
4. Federal University of São Carlos, Center for the Development of Functional Materials, São Carlos, Brazil.

+Corresponding author: Letícia Guerreiro da Trindade, **Phone:** +551633518214, **Email address:** lgt.gtrindade@gmail.com

ARTICLE INFO

Article history:
Received: July 05, 2021
Accepted: November 23, 2021
Published: April 11, 2022

Section Editors: Elson Longo and Juan Manuel Andrés Bort

Keywords:
1. Zr-MOF
2. solar cells
3. photoelectrode
4. photoelectrochemical properties

ABSTRACT: In this work, we investigated the effect of the coupling of the Zr-metal-organic framework (MOF) and SnO_2 and its potential for application as photoelectrode in solar cells. Coupling was performed by mechanical mixture followed by heat treatment. The effect of adding two amounts of Zr-MOF (25 and 50 wt%) on morphology and photoelectrochemical properties was investigated. The results of the J-V curves show that the coupling of 25 wt% Zr-MOF with SnO_2 improved the charge transfer characteristics under light irradiated in 1.6 times compared to the pure SnO_2.

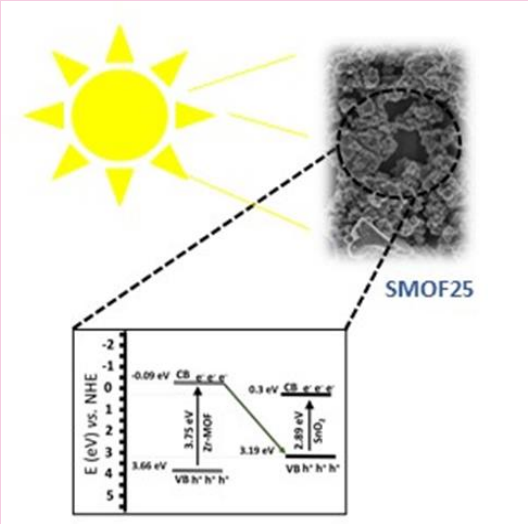

ISSN: 1678-4618
DOI: 10.26850/1678-4618eqj.v47.1SI.2022.p120-129

1. Introduction

Due to the scarcity of natural resources, the current technological society faces great challenges in relation to its own sustainability (Zhang and Sun, 2019). As a result, the demand for new clean and efficient technologies with lower environmental costs is growing. In this context, solar energy technology stands out, which can be easily found on almost the entire planet.

Research involving solar energy conversion into electricity has drawn a lot of attention, especially in photovoltaic devices such as solar cells (Kojima *et al.*, 2009). Among them, dye-sensitized solar cells (DSSCs) stand out for their low cost and simple fabrication method (Bora *et al.*, 2018; Chen *et al.*, 2018). However, such devices have low power conversion efficiency (PCE), which represents a barrier to the use of these devices in the photovoltaic market (Bashar *et al.*, 2019; Selvaraj *et al.*, 2018). Low PCE is related to the electronic, morphological and optical properties of materials used as photoanodes.

Currently, the most used n-type metal oxide as photoanode in DSSC is TiO_2 (Agbo *et al.*, 2016; Bhogaita *et al.*, 2016). Nevertheless, its material displays some deficiencies, such as low electron mobility and photic instability (W. Yang *et al.*, 2017). In addition, to removing organic compounds of the TiO_2 synthesis of it, it is necessary to use high temperatures, which results in higher production costs (W. Yang *et al.*, 2017). A great candidate to replace the conventional TiO_2 layer is the SnO_2 (Jiang *et al.*, 2017; Ke *et al.*, 2015) due to its wide bandgap, high optical transmittance in the visible, high mobility (240 $cm^2\ V^{-1}\ s^{-1}$), excellent optical and chemical stability, and low-cost preparation at low temperature (Mathiazhagan *et al.*, 2020). However, as the SnO_2 conduction band-edge is more positive than TiO_2 (~ 400 mV), under 1 Sun simulated light (AM 1.5 G) using a solar simulator, the Fermi quasi-equilibrium level will shift down to the redox potential of the liquid electrolyte, resulting in a lower open-circuit voltage compared to TiO_2 (Suresh *et al.*, 2018). These characteristics may make the DSSCs that use SnO_2 as photoanode achieve PCE of only 1.2% while DSSCs working with TiO_2 have a PCE of 5.9% (Concina and Vomiero, 2014). In order to overcome these limitations presented by SnO_2, an alternative found is the modification of its surface (Qian *et al.*, 2009).

The unique characteristics of the metal-organic frameworks (MOFs) such as high porosity, high surface area, accessible active internal energy migration pathways that can increase the electron transfer and reduce the charge recombination, have motivated research about their photocatalytic and photovoltaic applications (Zhang *et al.*, 2020). MOFs are hybrid materials built by combining the organic ligands and metal nodes through coordinate bonds (Bao *et al.*, 2016; H. Liu *et al.*, 2016; Li *et al.*, 2016).

Recently, our group investigated the coupling of ZnO and Zr-MOF to develop a photoanode to be applied in DSSCs. In this research, the results showed that the ZnO electrode with 25 wt% Zr-MOF has the ability to potentiate charge transport and inhibit charge recombination, making it a promising photoelectrode for solar cells (da Trindade *et al.*, 2021).

Based on our previous results, in this present work, we seek to report the investigation of the Zr-MOF/SnO_2 coupling in the SnO_2 morphology and its photoelectrochemical properties for future application in photoanodes for DSSCs.

2. Experimental

2.1 SnO_2 synthesis

The coprecipitation method in aqueous media was used to prepare the SnO_2 particles. In this method, $SnCl_2{\cdot}2H_2O$ (6.77 g, Vetec) was mixed with deionized H_2O (30 mL) under constant stirring at room temperature. After dissolution, H_2O_2 (35 mL, Synth) and KOH solution (35 mL/2 mol L^{-1}, Synth) were added. The precipitate was washed with deionized water until pH = 7. The obtained material was oven-dried at 60 °C for 8 h.

2.2 Zr-MOF synthesis

The metal-organic framework synthesis (Zr-MOF) was performed by a solvothermal method as related in our previous work (da Trindade *et al.*, 2019). The $ZrCl_4$ (1.4 mmol, Aldrich) and terephthalic acid (1.4 mmol, Aldrich) were previously dissolved in N, N-dimethylformamide (DMF, 99.8%, Aldrich) and the solution was put in an autoclave. The reaction was kept in a greenhouse at 125 °C for 24 h. After this time the obtained precipitate was washed with methanol and dried at 60 °C.

2.3 Electrode preparation

The electrodes were prepared with SnO_2 and Zr-MOF using two mass ratios of Zr-MOF, according to Tab. 1. The electrode preparation procedure was performed according to the literature (da Trindade *et*

Eclética Química Journal, vol. 47, special issue 1, 2022, 120-129
ISSN: 1678-4618
DOI: 10.26850/1678-4618eqj.v47.1SI.2022.p120-129

al., 2018; 2020a). Viscous pastes were prepared by mixing the desired particles with ethanol (200 µL) and sonicated for 30 min. After this, deionized water (60 µL) was added, and the mixture was sonicated again for 30 min. The obtained suspensions were applied onto fluorine-doped tin oxide (FTO) substrates in an area of 1 cm^2 using a micropipette. The films were allowed to dry at 25 °C for 1 h, and then calcined at 400 °C for 1 h, at heating and cooling rates of 0.1 °C min^{-1}.

Table 1. Samples designation and composition.

Sample designation	SnO_2 (g)	Zr-MOF (g)
SnO_2	0.0125	-
Zr-MOF	0.0125	-
SMOF25	0.0094	0.0031
SMOF50	0.0062	0.0062

2.4 Samples characterization

All samples were characterized by X-ray diffraction (XRD, Rigaku detector (CuKα, λ= 0.15406 nm), Fourier-transform infrared spectroscopy (FTIR, Bruker EQUINOX 55 spectrometer), thermogravimetry (TG) analysis (TA Instruments Q-50 apparatus), field emission gun–scanning electron microscope (FEG-SEM, ZEISS model 105 DSM940A instrument, 10 keV), UV–Vis spectra (Cary 5 G [Varian] apparatus) and Brunauer–Emmett–Teller (BET) surface area measurements (Micromeritics TriStar II 3020).

The photoelectrochemical measurements were performed in a three-electrode cell where the prepared electrode, Pt wire and Ag/AgCl electrode have been used as working, counter and reference electrodes, respectively. This cell had a quartz glass window, and the electrolyte was acetonitrile solution with LiI (10 mmol L^{-1}), I_2 (1 mmol L^{-1}), and $LiClO_4$ (0.1 mol L^{-1}). The current density-voltage (J-V) curves of the samples have been analyzed for both illuminated and dark conditions using an Autolab PGSTAT302 N potentiostat and a Newport Sol3A Class AAA solar simulator with a 100 W Xenon lamp.

3. Results and discussion

Figure 1 shows the XRD patterns of all samples. The SnO_2 presents 2θ diffraction angles at 26.4, 33.7, 37.8, 51.6, 54.2, 62.1, 65.5 and 78.6 degrees and (110), (101), (200), (211), (220), (310), (301) and (321) diffraction planes, respectively, corresponding to rutile structure (JCPDS nº: 41-1445) (Debataraja *et al.*, 2017). The Zr-MOF presents the XRD patterns that correspond with the Zr-MOF (UiO-66) reported previously (Luan *et al.*, 2015; da Trindade *et al.*, 2020b). When the SnO_2 sample is modified with 25 or 50 wt% of Zr-MOF, it can be observed that the referring to SnO_2 and an absorption peak appears between 5 and 10°, which confirms the presence of Zr-MOF in both samples. It is also possible to observe that in the 50 wt% sample the presence of other diffraction peaks referring to Zr-MOF. This result was expected since there was a significant increase in the Zr-MOF mass amount compared to the 25 wt% sample.

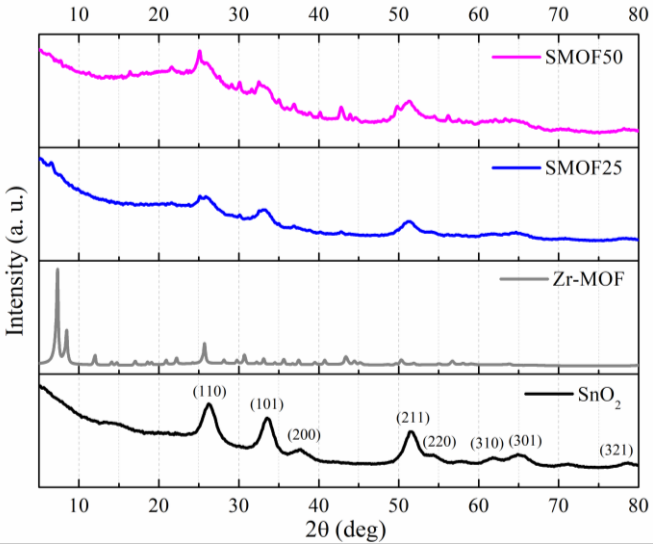

Figure 1. XRD patterns of SnO_2, Zr-MOF, SMOF25 and SMOF50 samples.

Figure 2 shows the FTIR and TG analyzes of SnO_2, Zr-MOF and modified samples. At the SnO_2 FTIR spectrum (Fig. 2a) we observed bands in 3300 and 1640 cm^{-1} that can be attributed to the O–H stretching of adsorbed water molecules. In addition, the band at 640 cm^{-1} refers to framework vibrations of SnO_2 (Zhan *et al.*, 2013). The Zr-MOF spectrum presents broadband at 3300 cm^{-1} that is due to the O–H stretching from water molecules in the MOFs (Zango *et al.*, 2020). The well-defined bands at 1570 and 1387 cm^{-1} refer to the C=O and C–N stretching modes, respectively. The C_{Ar}, δ-H stretching modes and the $Zr_6(OH)_4O_4$ cluster appears at 750 and 666 cm^{-1}, respectively (Butova *et al.*, 2020; da Trindade *et al.*, 2020b). For the modified samples, SMOF25 and SMOF50, similar spectra can be noted. Characteristic peaks of the SnO_2 and Zr-MOF were observed at both modified samples. However, the intensity of the bands increases with increasing the MOF amount in the sample. These results affirm that the Zr-MOF was successfully coupling into the SnO_2 corroborating the

Eclética Química Journal, vol. 47, special issue 1, 2022, 120-129
ISSN: 1678-4618
DOI: 10.26850/1678-4618eqj.v47.1SI.2022.p120-129

data observed by XRD. TG measurements were carried out to verify the thermal stability of SnO_2, Zr-MOF and modified samples (Fig. 2b). The pure SnO_2 sample presents only one stage of weight loss of 7% from 25 to 80 °C due to the removal of adsorbed water molecules. Zr-MOF has three stages of mass loss with first up to 125 °C which is attributed to desorption of physisorbed water, the second between 125−550 °C which may be due to the removal of the solvent (DMF) and the dehydroxylation of the zirconium oxo-clusters (X. Liu *et al.*, 2016) and the last stage (550-700 °C) is due to the Zr-MOF decomposition (Q. Yang *et al.*, 2018). When 25 wt % Zr-MOF is coupled to SnO_2 (SMOF25), it can be observed that there is an increase in thermal stability in relation to the pure SnO_2 sample. In the SMOF25 sample, there is an initial weight loss of approximately 3% that can be attributed to the removal of adsorbed water molecules. The increase in the initial thermal stability also is observed for the SMOF50 sample with a mass loss of 6%. However, at 500 °C the beginning of the Zr-MOF decomposition is observed. These data show that adding 25 wt % Zr-MOF to the SnO_2 sample works as a thermal stabilizer.

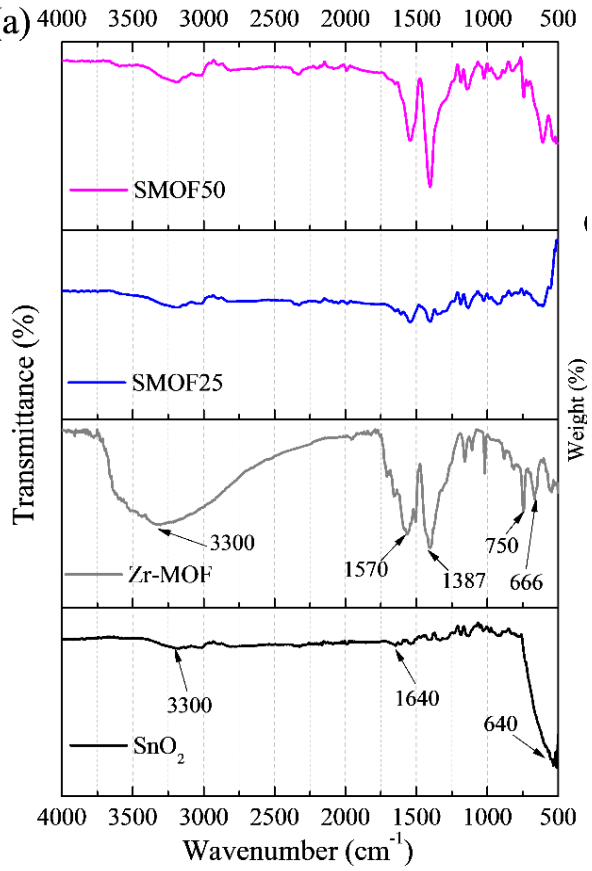

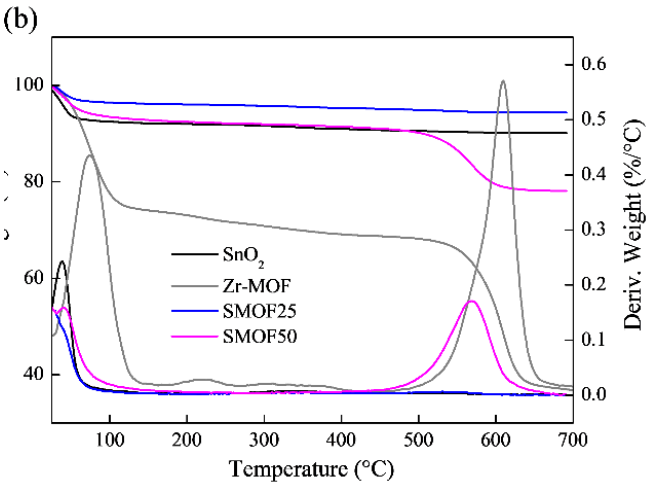

Figure 2. FTIR spectra **(a)** and TG curves **(b)** of SnO_2, Zr-MOF, SMOF25 and SMOF50 samples.

FE-SEM images for all samples are shown in Fig. 3. SnO_2 particles (Fig. 3a) tend to form agglomerates with irregular shapes. The Zr-MOF sample has an octahedral shape with different sizes as reported in the literature (Waitschat *et al.*, 2018). When 25 wt% Zr-MOF is coupled to the SnO_2 (Fig. 3c), there is a tendency to form clustered structures which are potentiated by increasing the Zr-MOF mass ratio (Fig. 3d). In the SMOF50 sample, the formation of agglomerates of smaller and fewer uniform particles is observed.

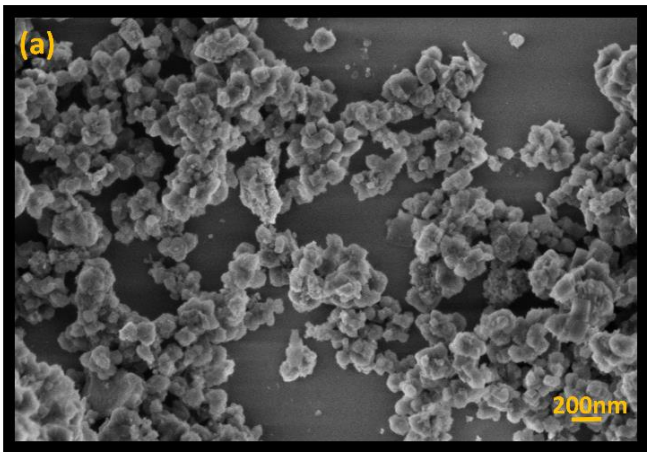

Eclética Química Journal, vol. 47, special issue 1, 2022, 120-129
ISSN: 1678-4618
DOI: 10.26850/1678-4618eqj.v47.1SI.2022.p120-129

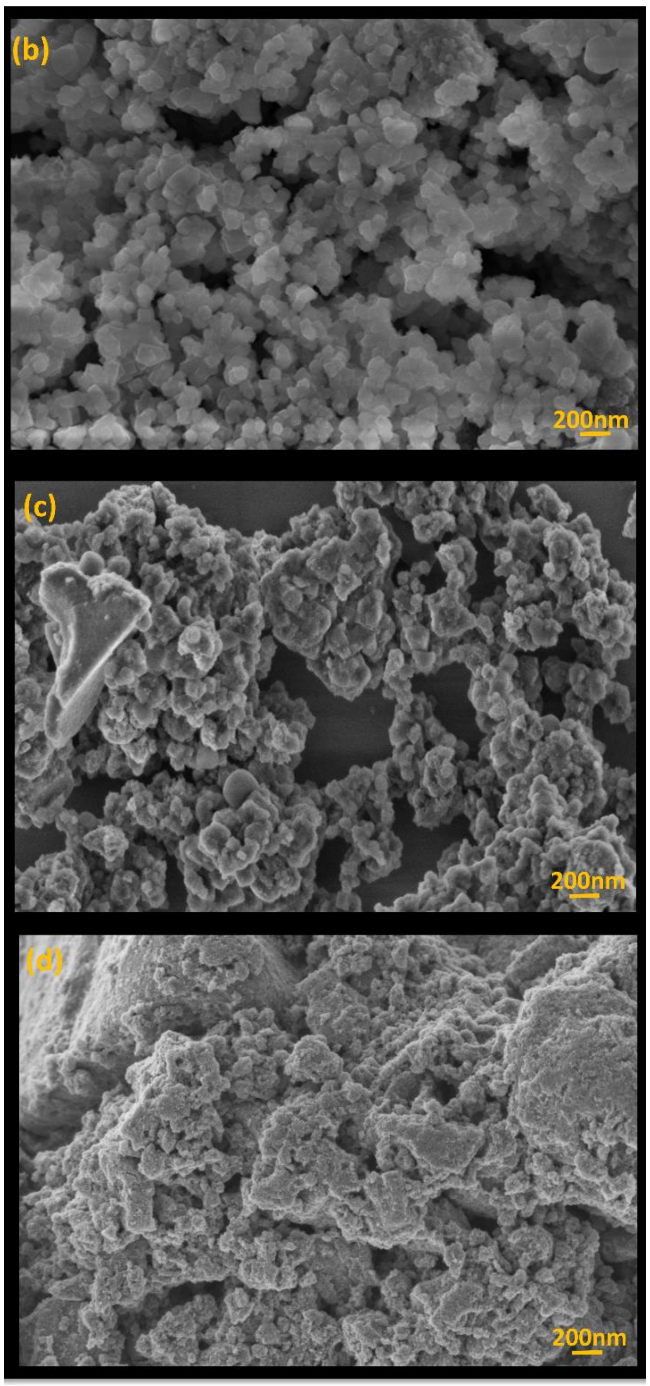

Figure 3. FE-SEM images of SnO_2 **(a)**, Zr-MOF **(b)**, SMOF25 **(c)**, and SMOF50 **(d)** samples.

Through the FE-SEM images, the particle size was estimated, Fig. 4a–d. The SnO_2 and the Zr-MOF samples present approximately 95.4 and 36 nm particle sizes, respectively. When these two samples are coupled, the particle sizes obtained are approximately 99.6 and 148.7 nm for SMOF25 and SMOF50 samples, respectively. These results reveal that the coupling of SnO_2 with Zr-MOF provokes an increase in particle size. The N_2 adsorption-desorption isotherms of SnO_2, Zr-MOF, SMOF25 and SMOF50 particles are shown in Fig. 4e. The SnO_2 and SMOF25 samples show typical type IV isotherms with a hysteresis loop and, the Zr-MOF and SMOF50 samples present typical type I isotherms. Type IV isotherms are characteristic of mesoporous nature and the hysteresis loop commonly suggests improved pore size and pore connectivity of the synthesized samples (Mallesham *et al.*, 2020). While type I isotherms indicate the microporous nature of the synthesized samples (Q. Yang *et al.*, 2018). It can be hypothesized that the reduction of the specific surface area with the addition of the Zr-MOF implies that the SnO_2/Zr-MOF coupling results in the reduction of the vacancies in the Zr-MOF (Fu *et al.*, 2019).

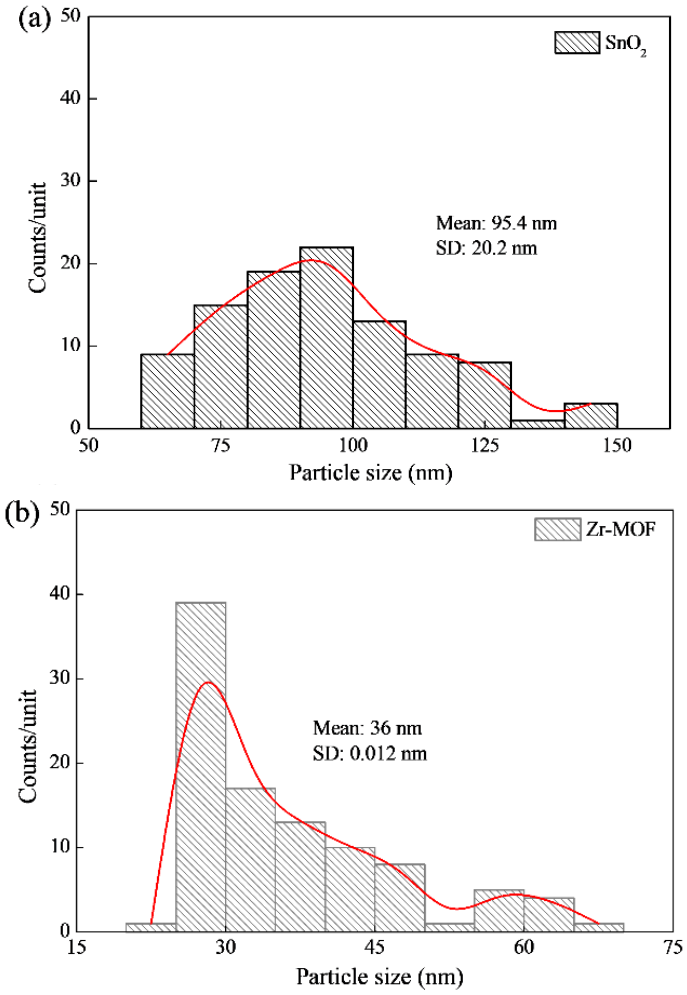

Eclética Química Journal, vol. 47, special issue 1, 2022, 120-129
ISSN: 1678-4618
DOI: 10.26850/1678-4618eqj.v47.1SI.2022.p120-129

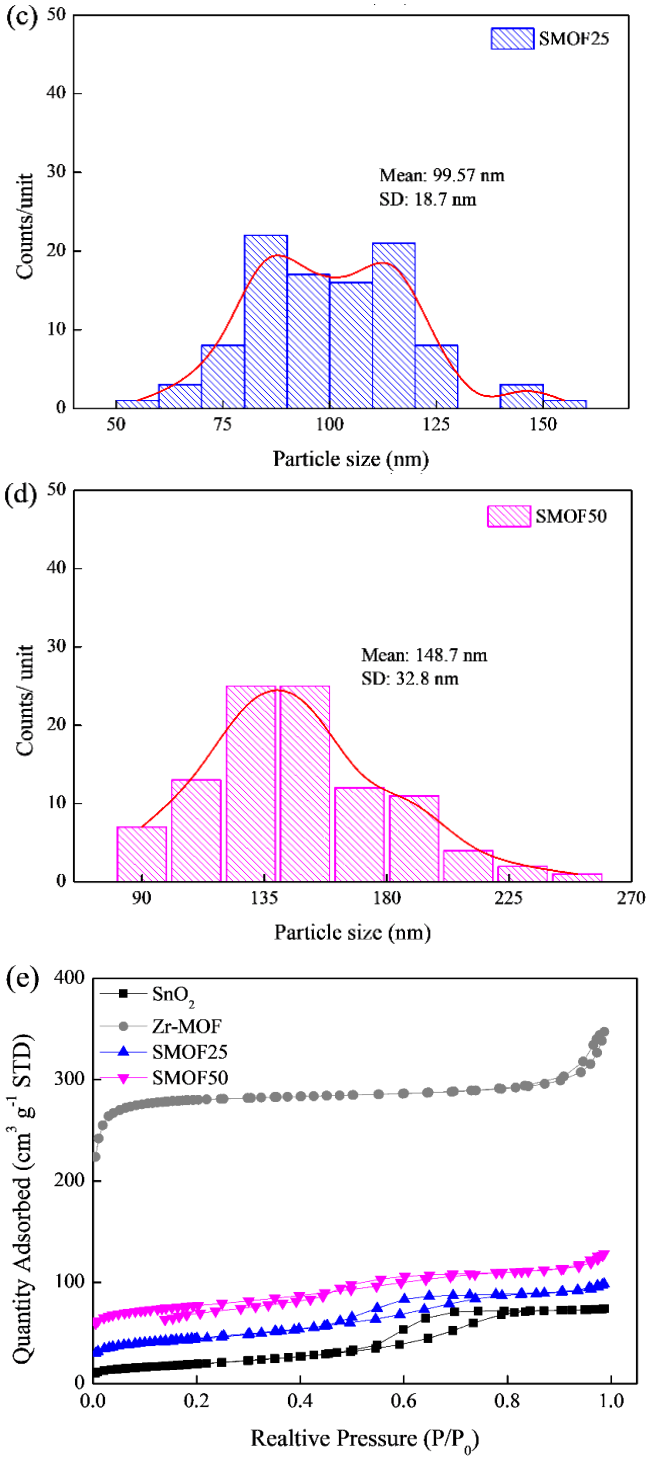

Figure 4. Particle sizes of SnO_2 **(a)**, Zr-MOF **(b)**, SMOF25 **(c)**, and SMOF50 **(d)**, and typical N_2 adsorption–desorption isotherm **(e)** of the samples.

The BET surface area and pore diameter are presented in Tab. 2. These results show that when SnO_2 is coupling with Zr-MOF the surface area increases from 68.44 $m^2\ g^{-1}$ to 158 and 270.3 $m^2\ g^{-1}$ with the addition of 25 and 50 wt% of Zr-MOF (SMOF25 and SMOF50), respectively. In contrast, the pore diameter decreases with coupling. These changes observed in the surface area and pore diameter can be caused by the increase of clusters formation as a result of the increase of the particles sizes.

Table 2. BET surface area and pore diameter, and FE-SEM average particle size of the samples.

Sample	BET		FE-SEM
	Surface area ($m^2\ g^{-1}$)	Pore diameter (nm)	Average particle size (nm)
SnO_2	68.44	4.5	95.4
Zr-MOF	985.2	10.0	36.0
SMOF25	158.0	4.3	99.6
SMOF50	270.3	3.4	148.7

The Tauc method was used to determining the bandgap (Coulter *et al.*, 2017), Eq. 1:

$$(\alpha h\nu)^{1/n} = A(h\nu - E_g) \quad (1)$$

where h is Planck's constant, ν is the photon's frequency, α is the absorption coefficient, E_g is the bandgap, and A is the slope of the Tauc plot in the linear region.

The SnO_2 and Zr-MOF are direct bandgap semiconductors with n equal to 1/2 (Ganose and Scanlon, 2016; Hendrickx *et al.*, 2018). The E_g values for all samples are shown in Fig. 5. The bandgap values are 2.89, 3.75, 2.27 and 2.12 eV for SnO_2, Zr-MOF, SMOF25 and SMOF50 samples, respectively. It can be seen that the bandgap is reduced with increasing in Zr-MOF concentration coupled to SnO_2. This behavior can be explained by factors like particle size, optical properties and surface morphology, which influence the penetration of light photons (da Trindade *et al.*, 2021).

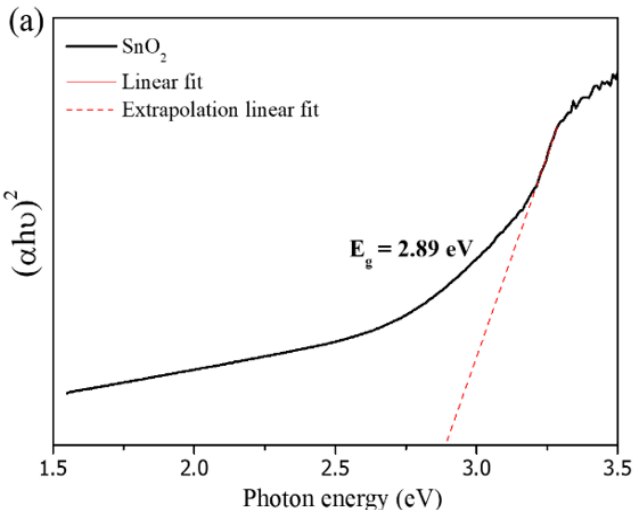

Eclética Química Journal, vol. 47, special issue 1, 2022, 120-129
ISSN: 1678-4618
DOI: 10.26850/1678-4618eqj.v47.1SI.2022.p120-129

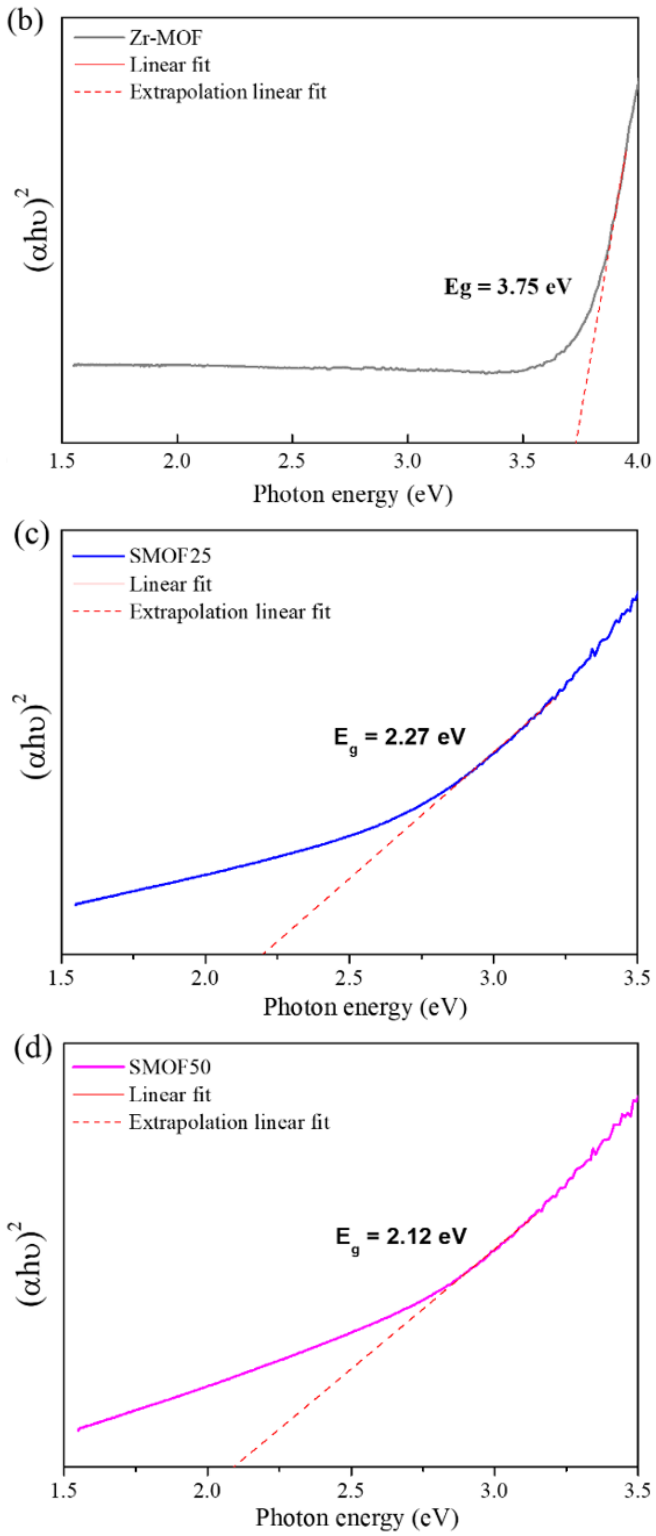

Figure 5. Tauc plot from UV-Vis analysis of SnO_2 **(a)**, Zr-MOF **(b)**, SMOF25 **(c)** and SMOF50 **(d)** samples.

The J-V curves of SnO_2, SMOF25 and SMOF50 photoanodes were analyzed in the potential range of 0–1.3 V at 20 mV s^{-1} in an I_3^-/I^- solution, Fig. 6. Current densities at 1.0 V in the presence of light are 2.77, 4.5 and 2.23 mA cm^{-2} for SnO_2, SMOF25 and SMOF 50, respectively. The results show that the coupling of 25 wt% Zr-MOF with SnO_2 improved the charge transfer characteristics under light irradiated compared to the pure SnO_2 and SMOF50 samples. The SMOF50 sample presented a current density lower than the other samples, indicating that 50 wt% Zr-MOF can reduce the active sites and delay the diffusion process for the electrolyte. This result demonstrates that the coupling of 25 wt% Zr-MOF with SnO_2 is promising for the development of photoanodes for DSSCs considering that the values of short-circuit density (Jsc), found in the literature, for the pure TiO_2 can range from 2.51 to 12.9 mA cm^{-2} (Concina and Vomiero, 2014; Khannam *et al.*, 2016). In the present work, the DSSC device was not assembled, we only tested the photoanode in I_3^-/I^- solution and without sensitized it by immersing in a dye solution. Therefore, by the obtained results, it is expected that when tested in the DSSC it will reach values similar or superior to cells with TiO_2.

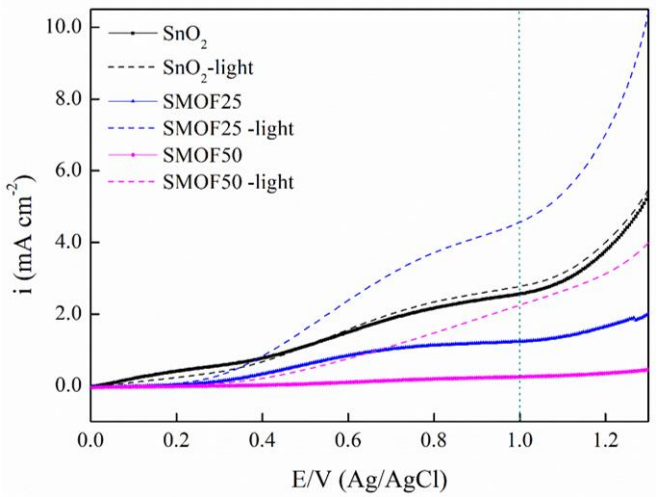

Figure 6. J-V curves of the SnO_2, Zr-MOF, SMOF25 and SMOF50 samples at 20 mV s^{-1}.

The valence band (E_{VB}) and conduction band (E_{CB}) potentials can be calculated by the Mulliken method, Eqs. 2 and 3, respectively (Kandasamy *et al.*, 2018):

$$E_{VB} = \chi - E_e + 0.5E_g \quad (2)$$

$$E_{CB} = E_{VB} - E_g \quad (3)$$

where χ is the electronegativity of the semiconductor and E_e is the energy of the free electrons on the hydrogen scale (4.5 eV) and E_g is the bandgap energy of the material.

Eclética Química Journal, vol. 47, special issue 1, 2022, 120-129
ISSN: 1678-4618
DOI: 10.26850/1678-4618eqj.v47.1SI.2022.p120-129

The SnO_2 electronegativity is 6.25 eV and the E_{CB} of Zr-MOF is –0.09 eV (vs. NHE); so, we can propose an energy band diagram for Zr-MOF coupling with SnO_2, Fig. 7 (Abdelkader *et al.*, 2015; Wang *et al.*, 2016). In the proposed energy band diagram when the SnO_2/Zr-MOF sample is exposed to visible light, the photogenerated electrons (e^-) in the Zr-MOF conduction band (CB) migrated to SnO_2, while the holes (h^+) remained in the Zr-MOF valence band (VB), resulting in the separation of the charge carriers.

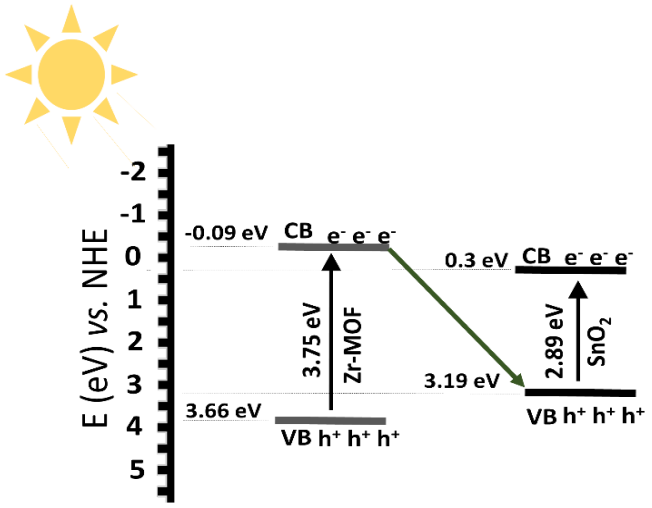

Figure 7. Proposed energy band diagram of the SnO_2/Zr-MOF composite.

4. Conclusions

The Zr-MOF coupling in the SnO_2 was prepared by mechanical mixture followed by heat treatment. The effect of the coupling has been investigated using structural, optical and photoelectrochemical analysis. The XRD and the FTIR reveals the incorporation of Zr-MOF into the SnO_2 lattice. The FE-SEM characterization shows an increase in the tendency to form clusters with an increase in the Zr-MOF concentration. The J-V data show that the coupling of 25 wt% Zr-MOF with SnO_2 improved 1.6 times the charge transfer characteristics under light irradiated compared to the pure SnO_2 and 2 times when compared to the SMOF50 sample. This result demonstrates that the coupling of 25 wt% Zr-MOF with SnO_2 is promising for the development of photoanodes for DSSCs.

Authors' contribution

Conceptualization: da Trindade, L. G.
Data curation: Silva, B. L. Z.; da Trindade, L. G.
Formal Analysis: Silva, B. L. Z.; da Trindade, L. G.; Zanchet, L.
Funding acquisition: Not applicable.
Investigation: da Trindade, L. G.
Methodology: da Trindade, L. G.; Mazzo, T. M
Project administration: Mazzo, T. M.; da Trindade, L. G.
Resources: Longo, E.
Software: Not applicable.
Supervision: Mazzo, T. M.
Validation: da Trindade, L. G.
Visualization: da Trindade, L. G.
Writing – original draft: da Trindade, L. G.; Zanchet, L.
Writing – review & editing: Mazzo, T. M.; Longo, E.; da Trindade, L. G.

Data availability statement

The data will be available upon request.

Funding

Conselho Nacional de Desenvolvimento Científico e Tecnológico (CNPq). Grant No: 163342/2020-2.

Fundação de Amparo à Pesquisa do Estado de São Paulo (FAPESP). Grant No: 2013/07296-2.

Coordenação de Aperfeiçoamento de Pessoal de Nível Superior (CAPES). Finance Code: 001.

Acknowledgments

Not applicable.

References

Abdelkader, E.; Nadjia, L.; Ahmed, B. Preparation and characterization of novel $CuBi_2O_4/SnO_2$ p–n heterojunction with enhanced photocatalytic performance under UVA light irradiation. *J. King Saud Univ. Sci.* **2015**, *27* (1), 76–91. https://doi.org/10.1016/j.jksus.2014.06.002

Agbo, S. N.; Merdzhanova, T.; Yu, S.; Tempel, H.; Kungl, H.; Eichel, R.-A.; Rau, U.; Astakhov, O. Photoelectrochemical application of thin-film silicon triple-junction solar cell in batteries. *Phys. Status Solidi A* **2016**, *213* (7), 1926–1931. https://doi.org/10.1002/pssa.201532918

Bao, C.; Zhou, L.; Shao, Y.; Wu, Q.; Zhu, H.; Li, K. A novel Au-loaded magnetic metal organic framework/graphene multifunctional composite: Green synthesis and catalytic

application. *J. Ind. Eng. Chem.* **2016**, *38*, 132–140. https://doi.org/10.1016/j.jiec.2016.04.014

Bashar, H.; Bhuiyan, M. M. H.; Hossain, M. R.; Kabir, F.; Rahaman, M. S.; Manir, M. S.; Ikegami, T. Study on combination of natural red and green dyes to improve the power conversion efficiency of dye sensitized solar cells. *Optik* **2019**, *185*, 620–625. https://doi.org/10.1016/j.ijleo.2019.03.043

Bhogaita, M.; Yadav, S.; Bhanushali, A. U.; Parsola, A. A.; Nalini, R. P. Synthesis and characterization of TiO_2 thin films for DSSC prototype. *Mater. Today: Proc.* **2016**, *3* (6), 2052–2061. https://doi.org/10.1016/j.matpr.2016.04.108

Bora, A.; Mohan, K.; Phukan, P.; Dolui, S. K. A low cost carbon black/polyaniline nanotube composite as efficient electro-catalyst for triiodide reduction in dye sensitized solar cells. *Electrochim. Acta* **2018**, *259*, 233–244. https://doi.org/10.1016/j.electacta.2017.10.156

Butova, V. V.; Vetlitsyna-Novikova, K. S.; Pankin, I. A.; Charykov, K. M.; Trigub, A. L.; Soldatov, A. V. Microwave synthesis and phase transition in UiO-66/MIL-140A system. *Microporous Mesoporous Mater.* **2020**, *296*, 109998. https://doi.org/10.1016/j.micromeso.2020.109998

Chen, L.; Chen, W.; Wang, E. Graphene with cobalt oxide and tungsten carbide as a low-cost counter electrode catalyst applied in Pt-free dye-sensitized solar cells. *J. Power Sources* **2018**, *380*, 18–25. https://doi.org/10.1016/j.jpowsour.2017.11.057

Concina, I.; Vomiero, A. Metal oxide semiconductors for dye- and quantum-dot-sensitized solar cells. *Small* **2014**, *11* (15), 1744–1774. https://doi.org/10.1002/smll.201402334

Coulter, J. B.; Birnie III, D. P. Assessing Tauc plot slope quantification: ZnO thin films as a model system. *Phys. Status Solidi B* **2017**, *255* (3), 1700393. https://doi.org/10.1002/pssb.201700393

da Trindade, L. G.; Minervino, G. B.; Trench, A. B.; Carvalho, M. H.; Assis, M.; Li, M. S.; Oliveira, A. J. A.; Pereira, E. C.; Mazzo, T. M.; Longo, E. Influence of ionic liquid on the photoelectrochemical properties of ZnO particles. *Ceram. Int.* **2018**, *44* (9), 10393–10401. https://doi.org/10.1016/j.ceramint.2018.03.053

da Trindade, L. G.; Borba, K. M. N.; Zanchet, L.; Lima, D. W.; Trench, A. B.; Rey, F.; Diaz, U.; Longo, E.; Bernardo-Gusmão, K.; Martini, E. M. A. SPEEK-based proton exchange membranes modified with MOF-encapsulated ionic liquid. *Mater. Chem. Phys.* **2019**, *236*, 121792. https://doi.org/10.1016/j.matchemphys.2019.121792

da Trindade, L. G.; Hata, G. Y.; Souza, J. C.; Soares, M. R. S.; Leite, E. R.; Pereira, E. C.; Longo, E.; Mazzo, T. M. Preparation and characterization of hematite nanoparticles-decorated zinc oxide particles (ZnO/Fe_2O_3) as photoelectrodes for solar cell applications. *J. Mater. Sci.* **2020a**, *55*, 2923–2936. https://doi.org/10.1007/s10853-019-04135-x

da Trindade, L. G.; Zanchet, L.; Dreon, R.; Souza, J. C.; Assis, M.; Longo, E.; Martini, E. M. A.; Chiquito, A. J.; Pontes, F. M. Microwave-assisted solvothermal preparation of Zr-BDC for modification of proton exchange membranes made of SPEEK/PBI blends. *J. Mater. Sci.* **2020b**, *55*, 14938–14952. https://doi.org/10.1007/s10853-020-05068-6

da Trindade, L. G.; Borba, K. M. N.; Trench, A. B.; Zanchet, L.; Teodoro, V.; Pontes, F. M. L.; Longo, E.; Mazzo, T. M. Effective strategy to coupling Zr-MOF/ZnO: Synthesis, morphology and photoelectrochemical properties evaluation. *J. Solid State Chem.* **2021**, *293*, 121794. https://doi.org/10.1016/j.jssc.2020.121794

Debataraja, A.; Zulhendri, D. W.; Yuliarto, B.; Nugraha; Hiskia; Sunendar, B. Investigation of nanostructured SnO_2 synthesized with polyol technique for CO gas sensor applications. *Procedia Eng.* **2017**, *170*, 60–64. https://doi.org/10.1016/j.proeng.2017.03.011

Fu, Y.; Wu, J.; Du, R.; Guo, K.; Ma, R.; Zhang, F.; Zhu, W.; Fan, M. Temperature modulation of defects in NH_2-UiO-66(Zr) for photocatalytic CO_2 reduction. *RSC Adv.* **2019**, *9*, 37733-37738. https://doi.org/10.1039/C9RA08097J

Ganose, A. M.; Scanlon, D. O. Band gap and work function tailoring of SnO_2 for improved transparent conducting ability in photovoltaics. *J. Mater. Chem. C* **2016**, *4* (7), 1467-1475. https://doi.org/10.1039/C5TC04089B

Hendrickx, K.; Joos, J. J.; De Vos, A.; Poelman, D.; Smet, P. F.; Van Speybroeck, V.; Van Der Voort, P.; Lejaeghere, K. Exploring lanthanide doping in UiO-66: A combined experimental and computational study of the electronic structure. *Inorg. Chem.* **2018**, *57* (9), 5463–5474. https://doi.org/10.1021/acs.inorgchem.8b00425

Jiang, Q.; Zhang, L.; Wang, H.; Yang, X.; Meng, J.; Liu, H.; Yin, Z.; Wu, J.; Zhang, X.; You, J. Enhanced electron extraction using SnO_2 for high-efficiency planar-structure $HC(NH_2)_2PbI_3$-based perovskite solar cells. *Nat. Energy* **2017**, *2*, 16177. https://doi.org/10.1038/nenergy.2016.177

Kandasamy, M.; Seetharaman, A.; Sivasubramanian, D.; Nithya, A.; Jothivenkatachalam, K.; Maheswari, N.; Gopalan, M.; Dillibabu, S.; Eftekhari, A. Ni-doped SnO_2 nanoparticles for sensing and photocatalysis. *ACS Appl. Nano Mater.* **2018**, *10* (1), 5823–5836. https://doi.org/10.1021/acsanm.8b01473

Ke, W.; Fang, G.; Liu, Q.; Xiong, L.; Qin, P.; Tao, H.; Wang, J.; Lei, H.; Li, B.; Wan J.; Yang, G.; Yan. Y. Low-temperature solution-processed tin oxide as an alternative electron transporting layer for efficient perovskite solar cells.

J. Am. Chem. Soc. **2015**, *137* (21), 6730–6733. https://doi.org/10.1021/jacs.5b01994

Khannam, M.; Sharma, S.; Dolui, S.; Dolui, S. K. Graphene oxide incorporated TiO_2 photoanode for high efficiency quasi solid state dye sensitized solar cells based on poly-vinyl alcohol gel electrolyte. *RSC Adv.* **2016**, *6*, 55406-55414. https://doi.org/10.1039/C6RA07577K

Kojima, A.; Teshima, K.; Shirai, Y.; Miyasaka, T. Organometal halide perovskites as visible-light sensitizers for photovoltaic cells. *J. Am. Chem. Soc.* **2009**, *131* (17), 6050–6051. https://doi.org/10.1021/ja809598r

Li, Y.; Xu, H.; Ouyang, S.; Ye, J. Metal–organic frameworks for photocatalysis. *Phys. Chem. Chem. Phys.* **2016**, *18* (11), 7563–7572. https://doi.org/10.1039/C5CP05885F

Liu, H.; Ren, X.; Chen, L. Synthesis and characterization of magnetic metal–organic framework for the adsorptive removal of Rhodamine B from aqueous solution. *J. Ind. Eng. Chem.* **2016**, *34*, 278–285. https://doi.org/10.1016/j.jiec.2015.11.02

Liu, X.; Zhao, X.; Zhou, M.; Cao, Y.; Wu, H.; Zhu, J. Highly stable and active palladium nanoparticles supported on a mesoporous UiO66@reduced graphene oxide complex for practical catalytic applications. *Eur. J. Inorg. Chem.* **2016**, *2016* (20), 3338−3343. https://doi.org/10.1002/ejic.201600367

Luan, Y.; Qi, Y.; Gao, H.; Andriamitantsoa, R. S.; Zheng, N.; Wang, G. A general post-synthetic modification approach of amino-tagged metal–organic frameworks to access efficient catalysts for the Knoevenagel condensation reaction. *J. Mater. Chem. A* **2015**, *3* (33), 17320–17331. https://doi.org/10.1039/C5TA00816F

Mallesham, B.; Rangaswamy, A.; Rao, B.G.; Rao, T. V.; Reddy, B. M. Solvent-free production of glycerol carbonate from bioglycerol with urea over nanostructured promoted SnO_2 catalysts. *Catal. Lett.* **2020**, *150*, 3626–3641. https://doi.org/10.1007/s10562-020-03241-9

Mathiazhagan, G.; Seeber, A.; Gengenbach, T.; Mastroianni, S.; Vak, D.; Chesman, A. S. R.; Gao, M.; Angmo, D.; Hinsch, A. Improving the stability of ambient processed, SnO_2-based, perovskite solar cells by the UV-treatment of sub-cells. *Sol. RRL* **2020**, *4* (9), 2000262. https://doi.org/10.1002/solr.202000262

Qian, J.; Liu, P.; Xiao, Y.; Jiang, Y.; Cao, Y.; Ai, X.; Yang, H. TiO_2-coated multilayered SnO_2 hollow microspheres for dye-sensitized solar cells. *Adv. Mater.* **2009**, *21* (36), 3663–3667. https://doi.org/10.1002/adma.200900525

Selvaraj, P.; Baig, H.; Mallick, T. K.; Siviter, J.; Montecucco, A.; Li, W.; Paul, M.; Sweet, T.; Gao, M.; Knox, A. R.; Sundaram, S. Enhancing the efficiency of transparent dye-sensitized solar cells using concentrated light. *Sol. Energy Mater. Sol. Cells* **2018**, *175*, 29–34. https://doi.org/10.1016/j.solmat.2017.10.006

Suresh, S.; Unni, G. E.; Satyanarayana, M.; Nair, A. S.; Pillai, V. P. M. Plasmonic $Ag@Nb_2O_5$ surface passivation layer on quantum confined SnO_2 films for high current dye-sensitized solar cell applications. *Electrochim. Acta* **2018**, *289*, 1–12. https://doi.org/10.1016/j.electacta.2018.08.078

Waitschat, S.; Fröhlich, D.; Reinsch, H.; Terraschke, H.; Lomachenko, K. A.; Lamberti, C.; Kummer, H.; Helling, T.; Baumgartner, M.; Henninger, S.; Stock, N. Synthesis of MUiO-66 (M = Zr, Ce or Hf) Employing 2,5-Pyridinedicarboxylic Acid as a linker: Defect chemistry, framework hydrophilisation and sorption properties. *Dalton. Trans.* **2018**, *47* (4), 1062–1070. https://doi.org/10.1039/C7DT03641H

Wang, A.; Zhou, Y.; Wang, Z.; Chen, M.; Sun, L.; Liu, X. Titanium incorporated with UiO-66(Zr)-type Metal–Organic Framework (MOF) for photocatalytic application. *RSC Adv.* **2016**, *6* (5), 3671–3679. https://doi.org/10.1039/C5RA24135A

Yang, W. S.; Park, B.-W.; Jung, E. H.; Jeon, N. J.; Kim, Y. C.; Lee, D. U.; Shin, S. S.; Seo, J.; Kim, E. K.; Noh, J. H.; Seok, S. I. Iodide management in formamidinium-lead-halide–based perovskite layers for efficient solar cells. *Science* **2017**, *356* (6345), 1376–1379. https://doi.org/10.1126/science.aan2301

Yang, Q.; Zhang, H.-Y.; Wang, L.; Zhang, Y.; Zhao, J. Ru/UiO-66 catalyst for the reduction of nitroarenes and tandem reaction of alcohol oxidation/knoevenagel condensation. *ACS Omega* **2018**, *3* (4), 4199−4212. https://doi.org/10.1021/acsomega.8b00157

Zango, Z. U.; Sambudi, N. S.; Jumbri, K.; Bakar, N. H. H. A.; Abdullah, N. A. F.; Negim, E.-S. M.; Saad, B. Experimental and molecular docking model studies for the adsorption of polycyclic aromatic hydrocarbons onto UiO-66(Zr) and NH_2-UiO-66(Zr) metal-organic frameworks. *Chem. Eng. Sci.* **2020**, *220*, 115608. https://doi.org/10.1016/j.ces.2020.115608

Zhan, S.; Li, D.; Liang, S.; Chen, X.; Li, X. A novel flexible room temperature ethanol gas sensor based on SnO_2 doped poly-diallyldimethylammonium chloride. *Sensors* **2013**, *13* (4), 4378–4389. https://doi.org/10.3390/s130404378

Zhang, B.; Sun, L. Artificial photosynthesis: Opportunities and challenges of molecular catalysts. *Chem. Soc. Rev.* **2019**, *48* (7), 2216–2264. https://doi.org/10.1039/C8CS00897C

Zhang, Y.; Mao, F.; Wang, L.; Yuan, H.; Liu, P. F.; Yang, H. G. Recent advances in photocatalysis over metal–organic frameworks-based materials. *Sol. RRL* **2020**, *4* (5), 1900438. https://doi.org/10.1002/solr.201900438

Eclética Química Journal, vol. 47, special issue 1, 2022, 120-129
ISSN: 1678-4618
DOI: 10.26850/1678-4618eqj.v47.1SI.2022.p120-129